Indoor Localization with Reconfigurable Intelligent Surface

Teng Ma, Yue Xiao, Xia Lei, Wenhui Xiong and Yuan Ding

***Abstract*—Recently, reconfigurable intelligent surface (RIS), which operates with the aim to manipulate multi-path signals, has been widely considered for wireless communications. In this letter, we extend the employment of RIS to indoor positioning, with the aid of ultra-wideband (UWB) technique. Moreover, the Cramér-Rao lower bound of the developed positioning scheme is quantified. Both theoretical analysis and simulation results demonstrate that RIS has the potential to realize accurate positioning with a single access point, due to its ability to mark the channel and replace traditional active positioning anchors. Moreover, it is also depicted that when the number of receive antennas is limited, time-of-arrival based positioning has a higher accuracy than that based on angle-of-arrival, due to the high multipath resolution of UWB signals.**

***Index Terms*—reconfigurable intelligent surface (RIS), ultra-wideband (UWB), positioning, Cramér-Rao lower bound (CRLB).**

I. Introduction

THE booming of reconfigurable intelligent surface (RIS) has aroused wide discussions in recent years as a promising technology for next-generation wireless communications [1]-[3]. Consisting of a large number of low-cost passive units that can reconfigure their physical parameters under the control of bias voltage [4], [5], RIS has been applied in many practical communication scenarios such as cell-edge communications, passive beamforming, etc., [6]-[8], to enhance the signal quality at receivers. Concretely, the authors of [1]-[3] summarized the evolution of RIS-assisted wireless communications, and disclosed the achievable transmission performance of the developed new systems. Moreover, the authors of [6] investigated the channel capacity of RIS-assisted communications systems, while the energy efficiency was studied in [7]. Furthermore, a class of novel RIS-assisted spatial modulation schemes [8] were developed with simplified implementation structure. Inspired by the freedom offered by RIS to manipulate wireless signals, we elaborate on the feasibility of employing RIS to increase the accuracy of indoor positioning.

T. Ma, Y. Xiao, X. Lei and W. Xiong are with the National Key Laboratory of Science and Technology on Communications, University of Electronic Science and Technology of China, 611731 Chengdu, China (Corresponding authors: Y. Xiao; X. Lei; Email: xiaoyue@uestc.edu.cn).

Y. Ding is with the Institute of Sensors, Signals and Systems (ISSS), Heriot-Watt University, Edinburgh, United Kingdom, EH14 4AS.

The financial support is gratefully acknowledged by the National Key R&D Program of China under Grant 2018YFB1800800, and the National Science Foundation of China under Grant number 61771106.

Conventional localization technology is prone to utilize Global Position System (GPS) signals or base stations (BSs) in the existing cellular networks to estimate the time of arrival (ToA), time-difference-of-arrival (TDoA) or angle-of-arrival (AoA) [9]-[12]. However, traditional positioning methods are not applicable indoors, due to the limited space size and abundant multipath environment. Meanwhile, the GPS signals and the signals from cellular BSs often suffer from blind areas, such as underground and various obstacles. Therefore, using wireless fidelity (WiFi) fingerprints, such as receive signal strength indication (RSSI), is a tendency for indoor positioning systems [13]-[15]. However, the precision of fingerprint-based positioning deeply depends on the accuracy of modeling the indoor propagation environment of electromagnetic waves.

Against this background, the authors of [16] studied WiFi-based indoor localization schemes in multiple-input multiple-output orthogonal frequency division multiplexing (MIMO-OFDM) systems, and discussed some deep learning based localization algorithms. Meanwhile, ultra-wideband (UWB) [17] and time-reversal [18] techniques, characterized by extremely high multipath resolution, have also attracted a lot of researches. Moreover, inspired by the Internet of Things (IoT) technologies, some researchers studied the schemes of multi-sensor cooperative positioning [19] and radio frequency identification devices (RFID) assisted positioning [20], at the cost of increased complexity for both hardware and network control. It is worth mentioning that there have been some attempts to utilize RIS into indoor positioning. For example, the authors of [21] investigated the Cramér-Rao lower bound (CRLB) of RIS-assisted positioning (RISP) using channel fingerprints. Meanwhile, the authors of [22] further developed a deep learning aided RISP algorithm based on [21]. However, to the best of the authors' knowledge, the current researches do not take full advantage of the ability of RIS to tag multipath channels.

In this context, we develop a novel indoor RISP scheme, for bridging the ability of RIS to label multipath channels and the high multipath resolution of UWB signals. Moreover, in order to demonstrate the effectiveness of the above-mentioned structure, the CRLB is also quantified by theoretical analysis. Theoretical analysis and simulation results exhibit that RIS has the potential to realize accurate positioning with a single access point.

The remainder of this letter is organized as follows. In Section II, the system model of UWB-assisted RISP is introduced. In Section III, we analyze the CRLB of the position estimate for such system. Section IV presents

simulation results and comparisons. Finally, conclusions are given in Section V.

II. System Model

Assume that an RIS consists of K units with small size and far spacing to assist positioning, whose reflection coefficient vector is

$$\boldsymbol{\rho} = \rho[e^{\mathrm{j}\theta_1}, e^{\mathrm{j}\theta_2}, \ldots, e^{\mathrm{j}\theta_K}]^{\mathrm{T}}, \tag{1}$$

where ρ is real-valued. When the phases satisfy $\theta_1 \neq \theta_2 \neq \cdots \neq \theta_K \in [0, 2\pi)$, the multipath signals passing through each RIS unit can be tagged. Considering that a transmitter uses a single antenna to send a UWB signal $s(t) = p(t)e^{\mathrm{j}2\pi f_c t}$ to accomplish positioning task, where f_c is the carrier frequency and $p(t)$ is a real-valued baseband pulse with pulse length T_p. Fig. 1 gives an example of UWB signals.

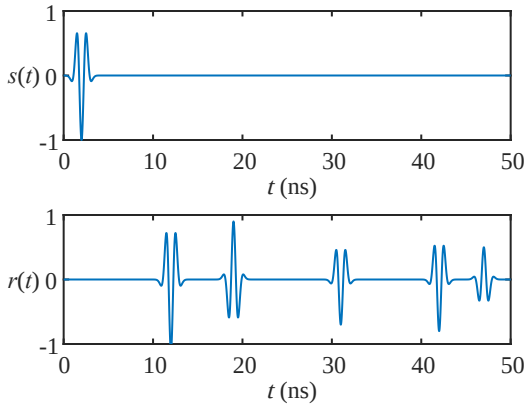

Fig. 1. An example of UWB signals (carrier, interference and noise are ignored).

Fig. 2 depicts the position-related parameters of the channel. These parameters include τ_{kl} and φ_{kl}, denoting the ToA and AoA of the lth path in P_k. Specifically, P_k is the set of resolvable multipath components from the transmitter to the kth RIS unit and to the receiver, and the cardinality of P_k is L_k. Meanwhile, we consider all the other resolvable multipath components between the transmitter and receiver that do not go through any RIS unit as P_0. We further denote the locations of the transmitter and RIS units as $\mathbf{p}_k = (x_k, y_k)^{\mathrm{T}}, k \in \{0, 1, 2, \cdots, K\} \overset{\text{def}}{=} \mathcal{K}$.

From the geometry shown in Fig. 1, we can obtain the relations between the parameters and positions, given by

$$\tau_{kl} = \frac{1}{c}(\|\mathbf{p}_k - \mathbf{p}_0\|_2 + \|\mathbf{p} - \mathbf{p}_k\|_2) + \xi_{kl}, \tag{2}$$

and

$$\varphi_{kl} = \tan^{-1}\frac{y - y_k}{x - x_k} + \psi_{kl}, \tag{3}$$

where c is the light speed, $\mathbf{p} = (x, y)^{\mathrm{T}}$ denotes the receiver position to be estimated, ξ_{kl} and $\psi_{kl}(l \in \{1, 2, \ldots, L_k\})$ are the unknown non-line-of-sight (NLoS) propagation-induced ToA and AoA errors of the lth path in P_k, respectively. For convenience, we assume that $\xi_{k1} < \xi_{k2} < \cdots < \xi_{kL_k}$. Suppose that line-of-sight (LoS) path exists

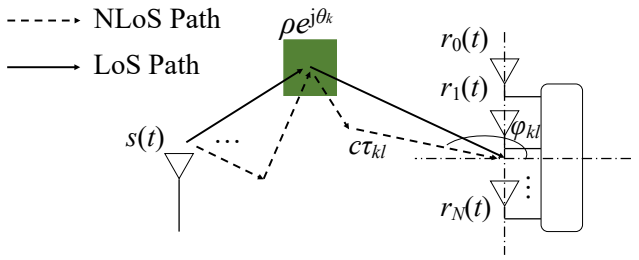

Fig. 2. Link topology of P_k in the RIS-assisted positioning system.

in $P_k (k \in \mathcal{L})$, where $\mathcal{L}$ is a subset of $\mathcal{K}$, hence we have $\xi_{k1} = \psi_{k1} = 0$. Then, the entire parameters to be estimated can be defined as

$$\boldsymbol{\eta} \overset{\text{def}}{=} [\mathbf{p}^{\mathrm{T}}, \boldsymbol{\xi}^{\mathrm{T}}, \boldsymbol{\psi}^{\mathrm{T}}]^{\mathrm{T}} = [\mathbf{p}^{\mathrm{T}}, \boldsymbol{\xi}_0^{\mathrm{T}}, \cdots, \boldsymbol{\xi}_K^{\mathrm{T}}, \boldsymbol{\psi}_0^{\mathrm{T}}, \ldots, \boldsymbol{\psi}_K^{\mathrm{T}}]^{\mathrm{T}}, \tag{4}$$

where

$$\boldsymbol{\xi}_k = \begin{cases} [\xi_{k2}, \xi_{k3}, \cdots, \xi_{kL_k}]^{\mathrm{T}}, & k \in \mathcal{L} \\ [\xi_{k1}, \xi_{k2}, \cdots, \xi_{kL_k}]^{\mathrm{T}}, & k \in \mathcal{K} - \mathcal{L} \end{cases} \tag{5}$$

and

$$\boldsymbol{\psi}_k = \begin{cases} [\psi_{k2}, \psi_{k3}, \cdots, \psi_{kL_k}]^{\mathrm{T}}, & k \in \mathcal{L} \\ [\psi_{k1}, \psi_{k2}, \cdots, \psi_{kL_k}]^{\mathrm{T}}, & k \in \mathcal{K} - \mathcal{L}. \end{cases} \tag{6}$$

Then, the Fisher information matrix (FIM) $\mathbf{F}_{\boldsymbol{\eta}}$ determines the CRLB of $\hat{\mathbf{p}}$, which is given by

$$\mathbf{C}_{\hat{\mathbf{p}}} = \left[\mathrm{E}(\hat{\boldsymbol{\eta}} - \boldsymbol{\eta})(\hat{\boldsymbol{\eta}} - \boldsymbol{\eta})^{\mathrm{T}}\right]_{2\times 2} \succeq [\mathbf{F}_{\boldsymbol{\eta}}^{-1}]_{2\times 2}, \tag{7}$$

where $[\cdot]_{m\times n}$ represents the upper left $m \times n$ submatrix. Meanwhile, the minimum mean squared error (MMSE) for the position estimates can also be obtained as

$$\mathrm{E}[\|\hat{\mathbf{p}} - \mathbf{p}\|_2^2] \geq \mathrm{tr}([\mathbf{F}_{\boldsymbol{\eta}}^{-1}]_{2\times 2}) \overset{\text{def}}{=} \varepsilon^2. \tag{8}$$

We further denote the channel response of P_k as

$$\mathbf{h}_k(t) = \rho e^{\mathrm{j}\theta_k} \sum_{l=1}^{L_k} \alpha_{kl} \boldsymbol{\beta}(\varphi_{kl}) \delta(t - \tau_{kl}), \tag{9}$$

where α_{kl} denotes the channel fading coefficient, $\boldsymbol{\beta}(\varphi_{kl}) \in \mathbb{C}^N$ is the antenna steering vector which depends on the specific array structure, and $\delta(t)$ is the Dirac function. In the context of a uniform linear array (ULA), we recall that

$$\beta_i(\varphi_{kl}) = e^{\mathrm{j}\frac{2\pi f_c}{c}(i - \frac{N-1}{2})\Delta \sin\varphi_{kl}}, i = 0, 1, \ldots, N-1, \tag{10}$$

where N is the number of the receive antennas, and Δ is the distance between antennas. A popular choice of Δ stands for half carrier wavelength, which is also considered in this letter. Thus, we can define

$$e^{\mathrm{j}\pi(i - \frac{N-1}{2})\sin\varphi_{kl}} \overset{\text{def}}{=} e^{\mathrm{j}(i - \frac{N-1}{2})\omega_{kl}} \overset{\text{def}}{=} \beta_i(\omega_{kl}). \tag{11}$$

Therefore, the received signal can be expressed as

$$\begin{aligned} \mathbf{r}(t) &= \rho \sum_{k=0}^{K} e^{\mathrm{j}\theta_k} \sum_{l=1}^{L_k} \alpha_{kl} \boldsymbol{\beta}(\omega_{kl}) s(t - \tau_{kl}) + \mathbf{r}_v(t) + \mathbf{n}(t) \\ &\overset{\text{def}}{=} \mathbf{y}(t|\boldsymbol{\alpha}, \boldsymbol{\tau}, \boldsymbol{\omega}) + \mathbf{n}'(t), \end{aligned} \tag{12}$$

where $\mathbf{v}(t)$ and $\mathbf{n}(t)$ are the unresolvable dense multipath components (DMC) interference and noise, respectively, while $\boldsymbol{\alpha} = [\boldsymbol{\alpha}_0^{\mathrm{T}}, \cdots, \boldsymbol{\alpha}_K^{\mathrm{T}}]^{\mathrm{T}}$, $\boldsymbol{\tau} = [\boldsymbol{\tau}_0^{\mathrm{T}}, \cdots, \boldsymbol{\tau}_K^{\mathrm{T}}]^{\mathrm{T}}$, $\boldsymbol{\omega} = [\boldsymbol{\omega}_0^{\mathrm{T}}, \cdots, \boldsymbol{\omega}_K^{\mathrm{T}}]^{\mathrm{T}}$, with $\boldsymbol{\alpha}_k = [\alpha_{k1}, \ldots, \alpha_{kL_k}]^{\mathrm{T}}$, $\boldsymbol{\tau} = [\tau_{k1}^{\mathrm{T}}, \cdots, \tau_{kL_k}^{\mathrm{T}}]^{\mathrm{T}}$, $\boldsymbol{\omega}_k = [\omega_{k1}, \ldots, \omega_{kL_k}]^{\mathrm{T}}$.

According to [23], DMC interference can be considered as a complex circular Gaussian random process. Meanwhile, for a conventional omni-directional antenna array, the DMC interference is uncorrelated for an antenna-spacing of half wavelength [24]. Thus, we can define $\mathbf{n}'(t)$ with each entry of $N_0/2$ bilateral power spectral density to denote the interference-plus-noise.

Note that only the channel-related parameters $\boldsymbol{\zeta} = [\boldsymbol{\alpha}^{\mathrm{T}}, \boldsymbol{\tau}^{\mathrm{T}}, \boldsymbol{\omega}^{\mathrm{T}}]^{\mathrm{T}}$ can be estimated directly, and the best estimate can be obtained by the Maximum A Posteriori (MAP) approach, namely

$$\hat{\boldsymbol{\zeta}} = \arg\max_{\boldsymbol{\zeta}} f\left(\mathbf{r}(t)|\boldsymbol{\zeta}\right) p(\boldsymbol{\zeta}), \tag{13}$$

where

$$f\left(\mathbf{r}(t)|\boldsymbol{\zeta}\right) \propto \exp\left\{-\frac{1}{N_0}\int \|\mathbf{r}(t) - \mathbf{y}(t|\boldsymbol{\zeta})\|_2^2 \mathrm{d}t\right\}, \tag{14}$$

and $p(\boldsymbol{\zeta})$ is the prior probability distribution of $\boldsymbol{\zeta}$. Then, the FIM of $\boldsymbol{\eta}$ can be given by

$$\mathbf{F}_{\boldsymbol{\eta}} = \mathbf{J}_{\boldsymbol{\zeta}\boldsymbol{\eta}} \mathbf{F}_{\boldsymbol{\zeta}} \mathbf{J}_{\boldsymbol{\zeta}\boldsymbol{\eta}}^{\mathrm{T}} \tag{15}$$

where $\mathbf{J}_{\boldsymbol{\zeta}\boldsymbol{\eta}} = \partial \boldsymbol{\zeta}^{\mathrm{T}} / \partial \boldsymbol{\eta}$ denotes the Jacobian matrix for mapping $\boldsymbol{\zeta}$ to $\boldsymbol{\eta}$, while

$$\mathbf{F}_{\boldsymbol{\zeta}} = -\mathrm{E}\left[\frac{\partial^2 \ln f\left(\mathbf{r}(t)|\boldsymbol{\zeta}\right)}{\partial \boldsymbol{\zeta} \partial \boldsymbol{\zeta}^{\mathrm{T}}}\right] - \mathrm{E}\left[\frac{\partial^2 \ln p_{\boldsymbol{\zeta}}}{\partial \boldsymbol{\zeta} \partial \boldsymbol{\zeta}^{\mathrm{T}}}\right] \overset{\mathrm{def}}{=} \mathbf{F}'_{\boldsymbol{\zeta}} + \mathbf{P}_{\boldsymbol{\zeta}}. \tag{16}$$

III. Performance Analysis

In this section, we provide the derivation of the CRLB for the position estimate $\hat{\mathbf{p}}$. It is worth mentioning that $\boldsymbol{\alpha}$ is not only a function of the path length $c\boldsymbol{\tau}$, but also depends on the environment, which is not easily related to the geometry. Therefore, only ToAs and AoAs are taken into consideration while fading coefficients are treated as nuisance parameters in the position estimation. We further define $\check{\boldsymbol{\zeta}} = [\boldsymbol{\tau}^{\mathrm{T}}, \boldsymbol{\omega}^{\mathrm{T}}]^{\mathrm{T}}$, so the Jacobian matrix can be reduced to

$$\mathbf{J}_{\check{\boldsymbol{\zeta}}\boldsymbol{\eta}} = \begin{bmatrix} \mathbf{J}_{\boldsymbol{\tau}\mathbf{p}} & \mathbf{J}_{\boldsymbol{\omega}\mathbf{p}} \\ \mathbf{J}_{\boldsymbol{\tau}\boldsymbol{\xi}} & \mathbf{O} \\ \mathbf{O} & \mathbf{J}_{\boldsymbol{\omega}\psi} \end{bmatrix}. \tag{17}$$

Thus, $\mathbf{F}_{\boldsymbol{\eta}}$ can be obtained by

$$\mathbf{F}_{\boldsymbol{\eta}} \approx \mathbf{J}_{\check{\boldsymbol{\zeta}}\boldsymbol{\eta}} \mathbf{F}'_{\check{\boldsymbol{\zeta}}} \mathbf{J}_{\check{\boldsymbol{\zeta}}\boldsymbol{\eta}}^{\mathrm{T}} + \mathrm{diag}(\mathbf{O}, \mathbf{P}_{\boldsymbol{\xi}}, \mathbf{P}_{\psi}), \tag{18}$$

where

$$\mathbf{F}'_{\check{\boldsymbol{\zeta}}} = \begin{bmatrix} \mathbf{F}'_{\boldsymbol{\tau}} & \mathbf{F}'_{\boldsymbol{\omega}\boldsymbol{\tau}} \\ \mathbf{F}'_{\boldsymbol{\tau}\boldsymbol{\omega}} & \mathbf{F}'_{\boldsymbol{\omega}} \end{bmatrix}. \tag{19}$$

According to (14) and (16), we have

$$F'_{\tau_{kl}} = \frac{2N}{N_0}\int |\rho \alpha_{kl} \dot{s}(t)|^2 \mathrm{d}t = 8N\pi^2\kappa^2\gamma_{kl}, \tag{20}$$

$$\begin{aligned} F'_{\omega_{kl}} &= \frac{2}{N_0}\sum_{i=0}^{N-1}(i - \frac{N-1}{2})^2 \int |\rho \alpha_{kl} s(t)|^2 \mathrm{d}t \\ &= \frac{1}{6}N(N^2-1)\gamma_{kl}, \end{aligned} \tag{21}$$

and

$$F'_{\tau_{kl}\omega_{kl}} = \frac{2N}{N_0}\int \rho^2 |\alpha_{kl}|^2 \Re\{\dot{s}(t)s(t)\}\mathrm{d}t, \tag{22}$$

where

$$\gamma_{kl} = \frac{\int |\rho \alpha_{kl} s(t)|^2 \mathrm{d}t}{N_0}, \kappa^2 = \frac{\int f^2 |S(f)|^2 \mathrm{d}f}{\int |S(f)|^2 \mathrm{d}f} \tag{23}$$

denote the signal-to-interference-plus-noise ratio (SINR) of the lth component in P_k and the squared effective bandwidth of $s(t)$, respectively, with $S(f)$ being the Fourier transform of $s(t)$. Suppose that the baseband pulse is chosen from Gaussian high-order derivative pulses, we have $F'_{\tau_{kl}\omega_{kl}} = 0$. Meanwhile, the pulse length of a UWB signal is assumed to be small enough, such that $T_p \ll |\tau_{k_1 l_1} - \tau_{k_2 l_2}|$. Therefore, $\mathbf{F}'_{\check{\boldsymbol{\zeta}}}$ can be approximated to a diagonal matrix.

Moreover, as shown in the geometric relations in (2) and (3), the entries of $\mathbf{J}_{\check{\boldsymbol{\zeta}}\boldsymbol{\eta}}$ can also be figured out, i.e.,

$$\mathbf{J}_{\tau_{kl}\mathbf{p}} = \frac{1}{c}[\cos\phi_k, \sin\phi_k]^{\mathrm{T}}, J_{\tau_{kl}\xi_{kl}} = 1, \tag{24}$$

and

$$\mathbf{J}_{\omega_{kl}\mathbf{p}} = \frac{\pi\cos\varphi_{kl}}{d_k}[-\sin\phi_k, \cos\phi_k]^{\mathrm{T}}, J_{\omega_{kl}\psi_{kl}} = \pi\cos\varphi_{kl}, \tag{25}$$

where

$$\phi_k = \arctan\frac{y - y_k}{x - x_k}, d_k = \sqrt{(x-x_k)^2 + (y-y_k)^2}, \tag{26}$$

and other elements in $\mathbf{J}_{\check{\boldsymbol{\zeta}}\boldsymbol{\eta}}$ are equal to 0.

For further analysis, we consider a simplified scenario where only the first arriving signals are detected, namely, $L_k = 1$. Suppose that the cardinality of $\mathcal{L}$ is M, then $\boldsymbol{\xi}$ and $\boldsymbol{\psi}$ are reduced to $[\xi_{k_1}, \xi_{k_2}, \ldots, \xi_{k_{(K-M)}}]^{\mathrm{T}}$ and $[\psi_{k_1}, \psi_{k_2}, \ldots, \psi_{k_{(K-M)}}]^{\mathrm{T}}$, with $k_1 \neq k_2 \neq \cdots \neq k_{(K-M)} \in \mathcal{K} - \mathcal{L}$. Meanwhile, we can define $\boldsymbol{\tau}_N = [\tau_{k_1}, \tau_{k_2}, \ldots, \tau_{k_{(K-M)}}]^{\mathrm{T}}$ and $\boldsymbol{\tau}_L = [\tau_{n_1}, \tau_{n_2}, \ldots, \tau_{n_M}]^{\mathrm{T}} (n_1 \neq n_2 \neq \cdots \neq n_M \in \mathcal{L})$ to denote the ToAs of NLoS/LoS multipath components. $\boldsymbol{\omega}_N$ and $\boldsymbol{\omega}_L$ are defined similarly.

We first consider ToA-based positioning, i.e.,

$$\mathbf{F}_{\boldsymbol{\eta},\mathrm{ToA}} = \begin{bmatrix} \mathbf{J}_{\boldsymbol{\tau}\mathbf{p}} \mathbf{F}_{\boldsymbol{\tau}} \mathbf{J}_{\boldsymbol{\tau}\mathbf{p}}^{\mathrm{T}} & \mathbf{J}_{\boldsymbol{\tau}_N\mathbf{p}} \mathbf{F}_{\boldsymbol{\tau}_N} \\ \mathbf{F}_{\boldsymbol{\tau}_N} \mathbf{J}_{\boldsymbol{\tau}_N\mathbf{p}}^{\mathrm{T}} & \mathbf{F}_{\boldsymbol{\tau}_N} + \mathbf{P}_{\boldsymbol{\xi}} \end{bmatrix} \overset{\mathrm{def}}{=} \begin{bmatrix} \mathbf{A} & \mathbf{B} \\ \mathbf{B}^{\mathrm{T}} & \mathbf{C} \end{bmatrix}, \tag{27}$$

which gives the CRLB for position estimates, namely

$$[\mathbf{F}_{\boldsymbol{\eta},\mathrm{ToA}}^{-1}]_{2\times 2} = \mathbf{A}^{-1} + \mathbf{A}^{-1}\mathbf{B}(\mathbf{C} - \mathbf{B}^{\mathrm{T}}\mathbf{A}^{-1}\mathbf{B})^{-1}\mathbf{B}^{\mathrm{T}}\mathbf{A}^{-\mathrm{T}}. \tag{28}$$

Therefore, the MMSE is $\varepsilon_{\mathrm{ToA}}^2 = \mathrm{tr}([\mathbf{F}_{\boldsymbol{\eta},\mathrm{ToA}}^{-1}]_{2\times 2})$. When the prior knowledge of NLoS propagation-induced errors is unavailable, CRLB only depends on LoS components [9]. Thus, we can give a loose bound

$$\varepsilon_{L,\mathrm{ToA}}^2 = \mathrm{tr}[(\mathbf{J}_{\boldsymbol{\tau}\mathbf{p}} \mathbf{F}_{\boldsymbol{\tau}} \mathbf{J}_{\boldsymbol{\tau}\mathbf{p}}^{\mathrm{T}})^{-1}] = \frac{\mathrm{tr}(\mathbf{J}_{\boldsymbol{\tau}\mathbf{p}} \mathbf{F}_{\boldsymbol{\tau}} \mathbf{J}_{\boldsymbol{\tau}\mathbf{p}}^{\mathrm{T}})}{\det(\mathbf{J}_{\boldsymbol{\tau}\mathbf{p}} \mathbf{F}_{\boldsymbol{\tau}} \mathbf{J}_{\boldsymbol{\tau}\mathbf{p}}^{\mathrm{T}})}. \tag{29}$$

The CRLBs and MMSEs for AoA and hybrid ToA&AoA positioning can be obtained in a similar way.

IV. Simulations And Discussions

In the following, we consider an indoor environment of a square region with the side length of 10 meters, and consider the coordinates of its four vertices as $(0,0),(0,10),(10,0)$ and $(10,10)$, respectively. Assuming that the transmitter and receiver are located at $(1,1)$ and $(5,5)$, while RIS units are located at $(i,10), i \in \{0,1,\ldots,10\}$. To simplify the simulation, we consider $\gamma_k = \gamma_0$ with $\mathcal{L} = \{0,1,\ldots,M\}$. For $k \in \mathcal{K} - \mathcal{L}$, we assume $\xi_k \sim \mathcal{N}(\mu_\xi, \sigma_\xi^2)$ and $\psi_k \sim \mathcal{N}(\mu_\psi, \sigma_\psi^2)$, as described in [9] and [10].

Fig. 3 depicts the root of MMSE (ϵ) using different positioning approaches. Specifically, we set $\kappa = 0.5$GHz, $N = 4, \mu_\xi = 20$ns, $\sigma_\xi = 10$ns, $\mu_\xi = 0$, and $\sigma_\xi = \pi/4$. Fig. 3(a) shows the strict bounds whether a LoS path exists ($M = 0$ or 1), while Fig. 3(a) provides the strict and loose bounds with $M = 2$. It is shown that if there exists a LoS path, hybrid ToA&AoA positioning will depict a significant accuracy gain. Meanwhile, it is also worth mentioning that the position accuracy increases with the number of LoS links increasing, and ToA-based positioning provides much more accuracy than that based on AoA. These comments can be explained to some extent by the detailed expression of $\epsilon^2_{L,\text{ToA}}$ and $\epsilon^2_{L,\text{AoA}}$ given in (30). We first replace γ_k and d_k by γ_0 and $\bar{d}_k$, then we have $\epsilon^2_{L,\text{ToA}} \approx \frac{c^2/(8\kappa^2)}{MN\pi^2\gamma_0}$ and $\epsilon^2_{L,\text{AoA}} \approx \frac{6\bar{d}_k{}^2/(N^2-1)}{MN\pi^2\gamma_0}$. It is noted that the number N of receive antennas has a greater influence on AoA-based positioning, while ToA-based positioning is affected by the effective bandwidth κ. For UWB signals, κ is usually greater than 500 MHz, indicating that $c^2/(8\kappa^2)$ is quite small. Therefore, AoA-based positioning has to largely increase the number of receive antennas to obtain a comparable accuracy with ToA-based positioning.

For further analysis, we provide comparisons with virtual anchor (VA) assisted positioning (VAP) [25]. To make a fair comparison, only the first-order reflections are considered, without obstacles in these reflection paths, revealing that 5 paths can be seen as LoS paths. Meanwhile, the parameter settings are the same as in Fig. 3., and we consider hybrid ToA&AoA approach. It is shown that as M increases, RISP will gradually approach and exceed the performance of VAP. This is because the different locations of anchors give different d_ks and ϕ_ks. If the RIS units with LoS paths are located right on the reflection points, the performance bound of RISP will be identical to that of VAP. However, if the walls are not perfect mirrors, or there are some obstacles, VAP is not applicable any more while RISP is always suitable.

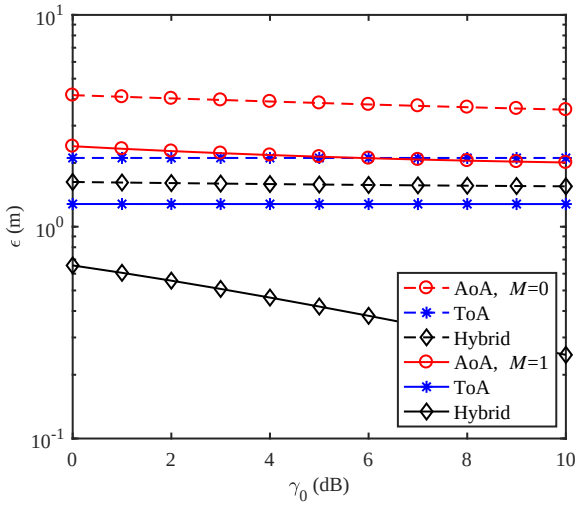

(a) Strict bounds with $M = 0$ and 1.

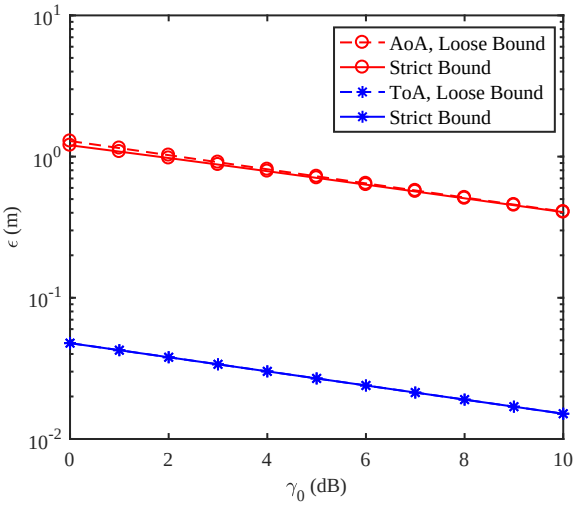

(b) Strict bounds and loose bounds with $M = 2$.

Fig. 3. Comparisons between different positioning approaches under different M.

In brief, we demonstrate that RIS has the potential to replace traditional active positioning anchors, i.e., access points and sensors, and provide an idea for multipath recognition in positioning. Moreover, toward an enhanced positioning accuracy, it is more beneficial to adopt ToA.

$$\varepsilon^2_{L,\text{ToA}} = \frac{c^2}{8N\pi^2\kappa^2} \frac{\sum_{k=0}^{M} \gamma_k}{(\sum_{k=0}^{M} \gamma_k \cos^2\phi_k)(\sum_{k=0}^{M} \gamma_k \sin^2\phi_k) - (\sum_{k=0}^{M} \gamma_k \sin\phi_k \cos\phi_k)^2},$$
$$\varepsilon^2_{L,\text{AoA}} = \frac{6}{\pi^2 N(N^2-1)} \frac{\sum_{k=0}^{M} \frac{\gamma_k}{d_k^2} \cos^2\phi_k}{(\sum_{k=0}^{M} \frac{\gamma_k}{d_k^2} \sin^2\phi_k \cos^2\phi_k)(\sum_{k=0}^{M} \frac{\gamma_k}{d_k^2} \cos^4\phi_k) - (\sum_{k=0}^{M} \frac{\gamma_k}{d_k^2} \sin\phi_k \cos^3\phi_k)^2}. \quad (30)$$

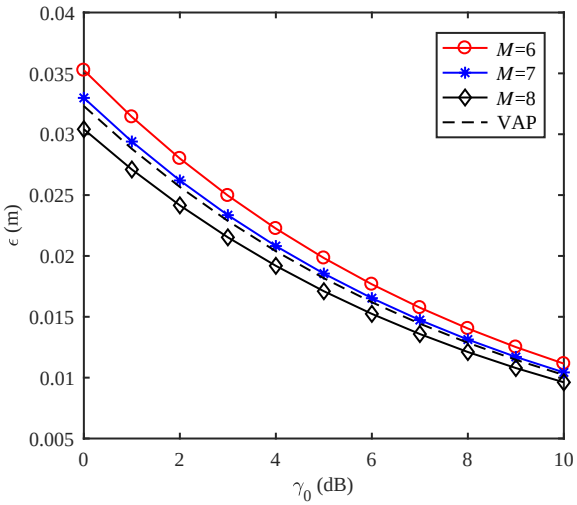

Fig. 4. Simulation comparisons of ϵ between different positioning approaches with $M = 0$ and 1.

V. Conclusions

In this letter, a general model for UWB-aided RIS-assisted indoor positioning has been developed and the CRLB of the position estimates has been derived. Specifically, RIS plays the role of marking the channel, while UWB signals are utilized for multipath recognition. Both theoretical derivations and simulation results demonstrated that the combination of RIS and UWB signals has the potential to realize accurate indoor positioning with a single access point. Moreover, compared with conventional single-physical-anchor positioning, i.e., using VAs, RISP shows a wider applicability. Furthermore, the proposed scheme achieves significant cost reduction, since it requires only a single access point and some low-cost RIS units. In this sense, the proposed scheme provides a more accurate and cost-effective solution for indoor positioning.

References

[1] E. Basar, M. Di Renzo, J. De Rosny, M. Debbah, M. Alouini, and R. Zhang, "Wireless communications through reconfigurable intelligent surfaces," *IEEE Access*, vol. 7, pp. 116753-116773, Aug. 2019.

[2] M. Di Renzo, M. Debbah, D. T. Phan-Huy, A. Zappone, M. S. Alouini, et al., "Smart radio environments empowered by reconfigurable AI meta-surfaces: An idea whose time has come," *EURASIP J. Wirel. Commun. Netw.*, vol. 2019:129, May 2019.

[3] E. Basar, "Transmission through large intelligent surfaces: A new frontier in wireless communications," in *Proc. European Conf. Netw. Commun. (EuCNC)*, Valencia, Spain, Jun. 2019, pp. 112-117.

[4] P. P. Kumar, K. Sreelakshmi, B. Sangeetha, and S. Narayan, "Metasurface based low profile reconfigurable antenna," in *Proc. 2017 International Conf. Commun. Signal Process. (ICCSP)*, Chennai, Apr. 2017, pp. 2081-2085.

[5] W. Tang, X. Li, J. Y. Dai, S. Jin, Y. Zeng, and Q. Cheng, "Wireless communications with programmable metasurface: Transceiver design and experimental results," *China Commun.*, vol. 16, no. 5, pp. 46-61, May 2019.

[6] Y. Han, W. Tang, S. Jin, C. Wen, and X. Ma, "Large intelligent surface-assisted wireless communication exploiting statistical CSI," *IEEE Trans. Veh. Technol.*, vol. 68, no. 8, pp. 8238-8242, Aug. 2019.

[7] C. Huang, A. Zappone, G. C. Alexandropoulos, M. Debbah, and C. Yuen, "Reconfigurable intelligent surfaces for energy efficiency in wireless communication," *IEEE Trans. Wirel. Commun.*, vol. 18, no. 8, pp. 4157-4170, Aug. 2019.

[8] E. Basar, M. Wen, R. Mesleh, M. Di Renzo, Y. Xiao and H. Haas, "Index modulation techniques for next-generation wireless networks," *IEEE Access*, vol. 5, pp. 16693-16746, 2017.

[9] Y. Qi, H. Kobayashi, and H. Suda, "On time-of-arrival positioning in a multipath environment," *IEEE Trans. Veh. Technol.*, vol. 55, no. 5, pp. 1516-1526, Sep. 2006.

[10] Y. Qi, H. Kobayashi, and H. Suda, "Analysis of wireless geolocation in a non-line-of-sight environment," *IEEE Trans. Wirel. Commun.*, vol. 5, no. 3, pp. 672-681, Mar. 2006.

[11] K. C. Ho and Y. T. Chan, "Solution and performance analysis of geolocation by TDOA," *IEEE Trans. Aerosp. Electron. Syst.*, vol. 29, no. 4, pp. 1311-1322, Oct. 1993.

[12] S. Venkatraman and J. Caffery, "Hybrid TOA/AOA techniques for mobile location in non-line-of-sight environments," in *Proc. 2004 IEEE Wirel. Commun. Netw. Conf. (IEEE Cat. No.04TH8733)*, Atlanta, GA, USA, 2004, pp. 274-278 Vol.1.

[13] H. Ahn and W. Yu, "Environmental-adaptive RSSI-based indoor localization," *IEEE Trans. Autom. Sci. Eng.*, vol. 6, no. 4, pp. 626-633, Oct. 2009.

[14] S. Mazuelas, A. Bahillo, R. M. Lorenzo, P. Fernandez, F. A. Lago, E.Garcia, J. Blas, and E. J. Abril, "Robust indoor positioning providedby real-time RSSI values in unmodified WLAN networks," *IEEE J. Sel.Topics Signal Process.*, vol. 3, no. 5, pp. 821-831, Oct. 2009.

[15] S. He and S. -. G. Chan, "Wi-Fi fingerprint-based indoor positioning: Recent advances and comparisons," *IEEE Commun. Surveys Tuts.*, vol. 18, no. 1, pp. 466-490, First quarter 2016.

[16] C. Xiang, et al., "Robust sub-meter level indoor localization with a single WiFi access point-regression versus classification,"*IEEE Access*, vol. 7, pp. 146309-146321, Oct. 2019.

[17] N. Patwari, J. N. Ash, S. Kyperountas, A. O. Hero, R. L. Moses, and N. S. Correal, "Locating the nodes: Cooperative localization in wireless sensor networks," *IEEE Signal Process. Mag.*, vol. 22, no. 4, pp. 54-69, Jul. 2005.

[18] G. C. Alexandropoulos, R. Khayatzadeh, M. Kamoun, Y. Ganghua, and M. Debbah, "Indoor time reversal wireless communication: Experimental results for localization and signal voverage," in *Proc. 2019 IEEE International Conference on Acoustics, Speech and Signal Processing (ICASSP)*, Brighton, United Kingdom, Apr. 2019, pp. 7844-7848.

[19] C. Huang, L. Lee, C. C. Ho, L. Wu, and Z. Lai, "Real-time RFID indoor positioning system based on Kalman-filter drift removal and Heron-Bilateration location estimation," *IEEE Trans. Instrum. Meas.*, vol. 64, no. 3, pp. 728-739, Mar. 2015.

[20] D. Dardari, A. Conti, U. Ferner, A. Giorgetti, and M. Z. Win, "Ranging with ultrawide bandwidth signals in multipath environments," in *Proc. IEEE*, vol. 97, no. 2, pp. 404-426, Feb. 2009.

[21] S. Hu, F. Rusek, and O. Edfors, "Beyond massive MIMO: The potential of positioning with large intelligent surfaces," *IEEE Trans. Signal Process.*, vol. 66, no. 7, pp. 1761-1774, 1 Apr. 2018.

[22] C. Huang, G. C. Alexandropoulos, C. Yuen, and M. Debbah, "Indoor signal focusing with deep learning designed reconfigurable intelligent surfaces," in *2019 IEEE 20th International Workshop on Signal Processing Advances in Wireless Communications (SPAWC)*, Cannes, France, Jul. 2019, pp. 1-5.

[23] J. Karedal, S. Wyne, P. Almers, F. Tufvesson, and A. Molisch, "A measurement-based statistical model for industrial ultra-wideband channels," *IEEE Trans. Wirel. Commun.*, vol. 6, no. 8, pp. 3028-3037, Aug. 2007.

[24] A. Paulraj, R. Nabar, and D. Gore, *Introduction to Space-Time Wireless Communications.* Cambridge, U.K.: Cambridge Univ. Press, 2003.

[25] M. Rath, J. Kulmer, E. Leitinger, and K. Witrisal, "Single-anchor positioning: Multipath processing with non-coherent directional measurements," *IEEE Access*, vol. 8, pp. 88115-88132, May 2020.